NTNU
Norwegian University of
Science and Technology

Study of FeSi Interlayers Formed During Iron-Mediated Epitaxial Growth of Graphene on SiC Substrates

Frode Sneve Strand

Master of Science in Physics and Mathematics
Submission date: August 2016
Supervisor: Justin Wells, IFY

Norwegian University of Science and Technology
Department of Physics

Abstract

A proposed graphene integrated semiconductor radiation sensor takes advantage of the electric field effect in graphene by measuring the change in resistance as a function of radiation exposure to the semiconductor substrate. The realisation of such radiation detectors requires that the controlled growth of graphene on wafer scale is possible. A possible production method is iron-mediated epitaxial graphene growth on silicon carbide (SiC) surfaces, where thin graphitic films can be synthesised by annealing. This technique has already been shown to lower the graphitisation temperature from around 1300° C to 600° C, whilst producing a FeSi interlayer as a by-product. A requirement for the operation of the aforementioned radiation sensor is that the graphene sheet is separated from the substrate by an insulator.

In this thesis, the FeSi interlayer was studied by growing epitaxial graphene from a Fe-treated SiC substrate, and tracking the evolution of the iron layer during annealing. The temperature at which the graphene and FeSi formation begins, and the quality of crystal structure as well as the properties of the resulting FeSi was studied by X-ray photoelectron spectroscopy (XPS), low-energy electron diffraction and microscopy (LEED and LEEM) and photoelectron diffraction (PED). The FeSi and thus graphene formation was found to begin at a temperature close to 390° C, which is a good improvement over graphene formation from a bare SiC surface, which occurs at around 1300°C. Moreover, the FeSi interlayer was found to take on a crystal structure commensurate to the SiC, thereby providing good conditions for high quality graphene formation on the surface. Last, the FeSi was found to be insulating, thus fulfilling the requirement for a working radiation sensor.

Sammendrag

En ny type strålingsdetektor som utnytter den elektriske felteffekten i grafén er foreslått. Realiseringen av en slik detektor forutsetter at produksjon av grafén i stor skala gjennomførbart. Tidligere har det blitt vist at ved å varme opp silisiumkarbid (SiC) til ca. 1300° C vil det dannes grafén på SiC-overflaten. Temperaturen der grafénet dannes kan senkes drastisk ved å dekke SiC-substratet med et tynt jernsjikt. Grafénet dannes da ved rundt 600° C på overflaten, og jernatomene binder opp silisiumatomer og danner FeSi, som blir sittende imellom substratet og grafénet. Den lavere temperaturen er mye mer tilgjengelig når en skal produsere grafén. Dersom FeSi-sjiktet er en elektrisk isolator, kan det brukes i den nevnte detektoren.

Derfor har vi i denne masteroppgaven undersøkt FeSi-sjiktet som dannes når en fremstiller epitaktisk grafén ved å utgløde jernbehandlet SiC. Vi har sett på hvilken temperatur graféndannelsen (og dermed FeSi-dannelsen) starter, i tillegg til krystalliniteten og ledningsegenskapene til FeSi, ved å benytte røntgenelektronspektroskopi, lavenergi-elektrondiffraksjon, lavenergi-electronmikroskopi samt fotoelektrondiffraksjon.

I eksperimentene ble begynnelsen av FeSi- og graféndannelsen observert ved rundt 390° C, noe som er mye lavere enn det som tidligere er observert ved rene SiC-overflater, der reaksjonen skjer rundt 1300° C. I tillegg fikk FeSi-sjiktet en krystallstruktur tilsvarende SiC-substratet under utglødingen, noe som er en forutsetning for at grafénet som dannes på overflaten skal få en krystallstruktur av høy kvalitet. Det ble til slutt vist at FeSi-sjiktet er isolerende, slik at forutsetningen for å lage en fungerende strålingsdetektor er oppfylt.

Preface

This Master's Thesis is the conclusion of a five year Applied Physics programme at the Norwegian University of Science and Technology. It is an integrated engineering and physics programme which results in a "Siv. ing." title. The work in this thesis was done under the supervision of associate professor Justin Wells in the section for condensed matter physics.

I would like to thank my supervisor, assoc. prof. Justin Wells, for all his help and patience when things were moving slowly, the good environment he provides for his research group, answering questions in the odd hours, and especially for bringing be to two synchrotron beamtimes! I have had a good time, and learned a lot. Dr. Simon Cooil deserves special thanks for his invaluable help in the lab and with the analysis. This thesis would never be finished otherwise. Lastly, I would like to thank all my classmates for all the good times we have had together as students here at NTNU.

Frode Sneve Strand
Trondheim, Norway
August 2016

Contents

1 Introduction

Graphene is a two-dimensional material composed of carbon atoms in a flat, hexagonal lattice structure. Since it was successfully isolated by Geim and Novoselov in 2004 [1], for which they were awarded the Nobel prize, graphene has seen an explosion in research interest and has revealed itself to have a great potential in technological applications [2]. Graphene has a range of unique properties resulting from its two-dimensional structure. It has a high mechanical strength [3], a high thermal conductivity [4] and a very high charge carrier mobility [5]. Arguably one of the most important properties of graphene is the unique electronic band structure. Graphene has a linear energy-momentum dispersion around the corners of the hexagonal Brillouin zone, which are also known as the K-points [6]. The top of the valence band and the bottom of the conduction band meet at the K-points, making graphene semimetallic. Moreover, due to the linear energy-momentum dispersion relationship, the charge carriers obey the Dirac equation for massless fermions, which means that they have an effective mass of zero at the K-points [7, 8]. For this reason, the K-points are also referred to as the Dirac points.

Graphene has a remarkably high charge carrier mobility at room temperature [2]. The electric conductivity in graphene is very sensitive to local electric fields due to a high difference in the carrier density at the Fermi level, see Figure 1.1. The position of the Fermi level can be shifted due to the electric field effect, effectively doping the graphene and increasing the carrier density and therefore the conductivity [1]. This sensitivity to electric fields could be used in devices for radiation sensing. A novel concept of graphene integrated semiconductor radiation detectors has been proposed which takes advantage of the rapid response of the conductivity to electric field variations [9]. A schematic view of such a detector can be seen in Figure 1.2. When a semiconductor substrate is exposed to ionising radiation, electron-hole pairs are produced that can migrate within the semiconductor. The electrons (or holes) are migrated towards

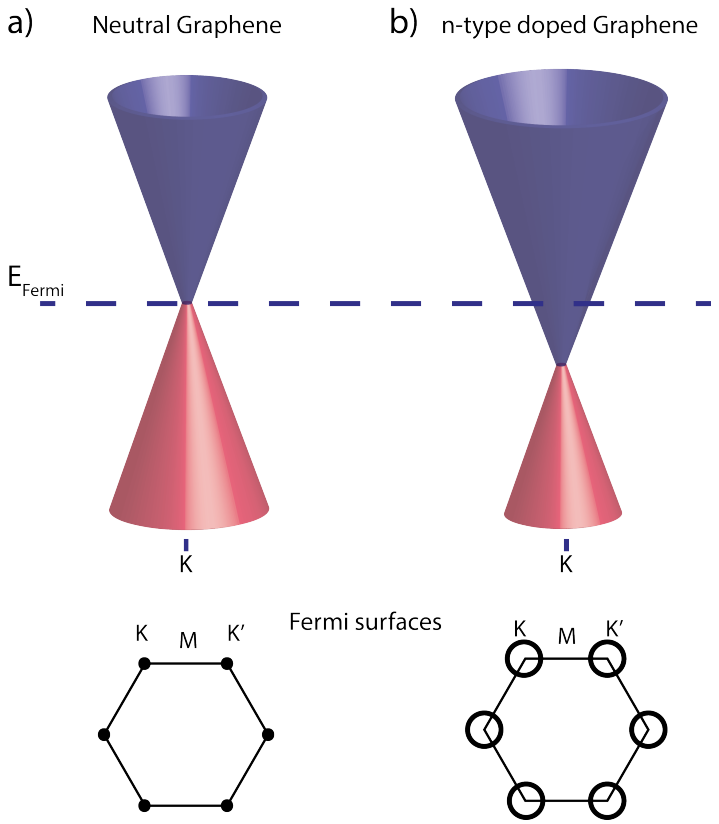

FIGURE 1.1: The conical band structure of graphene around the Dirac points (top) and the associated constant energy slices (bottom). The valence band is shown in red, and the conduction band is shown in blue. **a)** The Fermi level crosses exactly the Dirac points in neutral graphene, and the density of states (DOS) is very low, as indicated in the Fermi surface plot. **b)** n-type doped graphene displaying a shift in the band structure, leading to an increased carrier density.

the graphene sheet, which is separated from the semiconductor by a thin insulator. When the electrons are at the semiconductor-insulator interface, the electric field generated by the electrons shift the electronic band structure by an amount that depends on the strength of the electric field, and thus the number of electron-hole pairs that

was generated by the radiation (Figure 1.1). The band structure shift changes the charge carrier density in the graphene, which is detected by measuring the resistivity of the graphene. Simulations have shown that graphene integrated on the semiconductor surface is sensitive enough to detect the electric fields generated by an electron-hole pair created by a single photon interaction [9]. Primitive tests of this concept have shown good performance with visible light and soft x-rays [10, 11]. If the device structure and operation is optimised, one may reach unprecedented performance in terms of speed, resolution, sensitivity, etc.

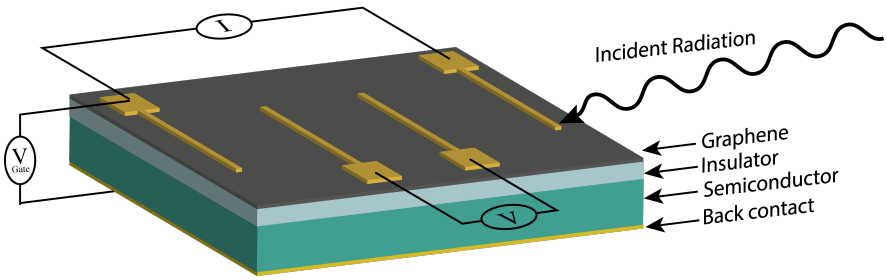

Figure 1.2: Proposed graphene field effect transistor (GFET) device. A semiconductor substrate is irradiated by ionising radiation, producing electron-hole pairs whose electric fields create a doping effect in the graphene which affects the resistivity. The four probes on the graphene surface are used to make resistivity measurements, allowing for change in resistance as a function of radiation exposure to be measured.

An important aspect of the realisation of such sensors is the manufacturing phase. In order to make it viable on the commercial market, an important requirement is that it is possible to produce high quality graphene sheets on a wafer scale. A promising technique is the epitaxial growth on silicon carbide (SiC) or diamond substrates, where ultrathin graphitic films can be synthesised by high-temperature annealing of the substrates [12, 13]. Diamond wafers can be grown by

chemical vapour deposition, and is getting cheaper [14]. It has been shown that the temperature at which graphene is formed can be lowered by a significant amount by coating the surface of the substrate with a thin layer of iron prior to annealing [15, 16]. In the case of SiC, the iron catalyst lowers the graphitisation temperature from ~1300° to ~600° C, whilst a FeSi interlayer is produced as a by-product [15]. SiC is a commercially available, wide-bandgap semiconductor which is very suitable for operation in high temperatures. Furthermore, SiC is chemically inert, which allows for operation in dangerous environments like high energy radiation areas [17]. Diamond is also very suitable for these environments, and whilst other semiconducting substrates with different properties may be used depending on what environment it will operate in or what type of radiation it will detect.

The aim of this project is to learn more about the FeSi interlayer during Fe-mediated graphene growth on SiC. Currently, the method is well understood in terms of the final graphene quality and electronic band structure, however there is a need to further study the SiC-FeSi-$C_{graphene}$ system if this method is to be used to create the aforementioned devices. A requirement for the operation of the devices is that the FeSi is sufficiently insulating to stop the charge carriers from entering the graphene sheet. Moreover, other iron-based compounds may be formed, for instance $FeSi_2$, Fe_3C [18].

To study the FeSi interlayer, photoemission techniques will be used, including X-ray photoelectron spectroscopy (XPS) for chemical information, photoelectron diffraction (PED) to measure the electronic structure of graphene, and low-energy electron diffraction and microscopy (LEED and LEEM) for structural and topographical analysis with high lateral resolution.

2 Experimental techniques

This chapter gives an introduction to the experimental techniques employed in this project. It should supply all the necessary base knowledge required to justify and understand the results of the experiments. The techniques discussed here are X-ray photoelectron spectroscopy (XPS), photoelectron diffraction (PED), low-energy electron diffraction (LEED) and low-energy electron microscopy (LEEM).

2.1 Principles of photoemission spectroscopy

Photoemission spectroscopy takes advantage of the photoelectric effect. When electromagnetic waves (typically X-rays) irradiate a material, they will interact with the electrons in the bulk of the sample. If the photons have energies greater than the sample work function, then electrons can be emitted into vacuum. In the most simple picture, the process can be described in terms of three steps [19]: the electron is excited to a higher energy state by the photon; the electron travels trough the crystal towards the surface; the electron escapes into vacuum. Photoelectrons usually have a mean-free path length of only a few nanometres within the sample, meaning that most of the photoelectrons that are detected originate from the atomic layers close to the surface, although photoelectrons from deeper in the sample may escape into vacuum if they undergo multiple inelastic scatterings [20].

In an XPS experiment, the sample is irradiated by X-rays which excite electrons such that they escape the sample into vacuum. The intensity of the emitted photoelectrons is measured as a function of kinetic energy. The kinetic energy (E_K) of the photoelectron is dependent on the incident photon energy ($h\nu$, h and ν being Planck's constant and the frequency, respectively), the binding energy (E_B) of the electron, and the characteristic work function (Φ_S) of the solid. The intensity ($I(E)$) is in turn dependent on the density of states (DOS)

of the electrons in the sample. Thus, in an XPS experiment, we gain information about the elements that are present in the sample as well as the chemical environment.

The relationship between E_K and $h\nu$ is, due to conservation of energy [21],

$$E_K = h\nu - E_B - \Phi_S. \tag{2.1}$$

This simple relationship can be readily seen in in Figure 2.1. In the Figure, the photon energy $h\nu$ relates the binding energy to the kinetic energy of the electrons that are measured by the analyser. It is common to plot the intensity against the binding energy rather than kinetic energy. In reality, most of the photoelectrons undergo inelastic scattering with other particles within the crystal, leading to a secondary electron tail with low kinetic energy [20], which is not reflected in the Figure.

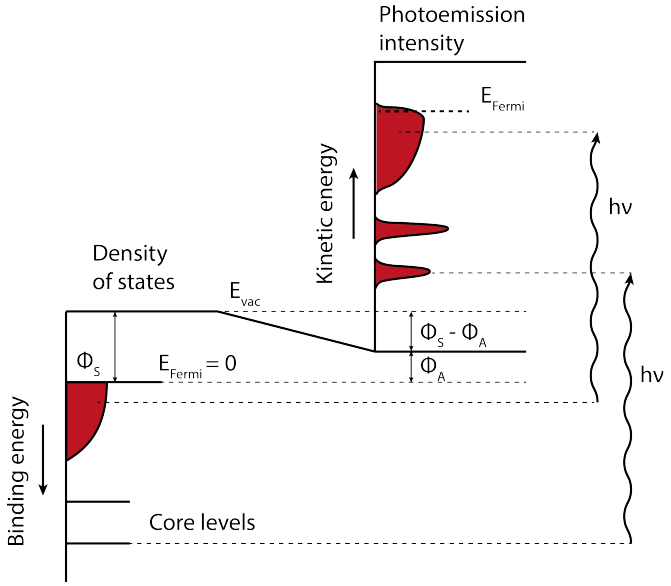

Figure 2.1: Energy diagram of the X-ray photoemission process. Electrons with a binding energy E_B are excited by X-rays with $h\nu > E_B + \Phi_A$, and the intensity $I(E_K)$ is measured by the analyser. The photoelectron distribution is an image of the occupied DOS in the sample, to first order [20, 22].

The analyser has its own work function Φ_A. An electrical connection is made between the sample and the analyser, which aligns the Fermi levels. This causes the measured kinetic energy to be offset by $\Phi_S - \Phi_A$, so the kinetic energy that is actually measured is given by [20]

$$\begin{aligned} E_K &= h\nu - E_B - \Phi_S + (\Phi_S - \Phi_A) \\ &= h\nu - E_B - \Phi_A. \end{aligned} \tag{2.2}$$

2.1.1 Features and interpretation of XPS spectra

There is a lot more to XPS than what is shown in Figure 2.1. Solids, being many-particle systems, affect the measured spectrum in a number of ways due to photoelectrons interacting within the solid and re-equilibration of the electronic states of the material. In addition, X-ray sources such as anode-based X-ray guns may give rise to satellite peaks due to the non-monochromatic nature of the generated X-rays (discussed in Chapter 3).

A survey spectrum (also called a widescan) of a clean SiC sample can be seen in Figure 2.2. The primary (and most obvious) features in the spectrum are the well-defined peaks arising from core-level electrons that escaped into vacuum without interacting with the crystal. The intensity of the core-level peaks depends on the photoionisation cross-section (the total probability of ionisation for a given photon energy) [23]. Each peak will always have a tail at lower kinetic energies due to photoelectrons that suffered energy losses in inelastic scattering events [24]. Plasmon loss peaks can occur when the photoelectron interacts with other electrons in the solid, giving rise to quantised oscillations in the valence states [22].

Auger peaks occur due to the Auger mechanism where the inner-shell vacancy left by the ejected photoelectron is filled by an electron from a higher orbital, ejecting a secondary electron in the process [25]. The kinetic energy of the Auger electron is independent of the photon energy used in the experiment, and it is characteristic of the emitting element. Thus, the Auger peaks will appear at different binding energies if the X-ray energy is changed. The Auger peaks can

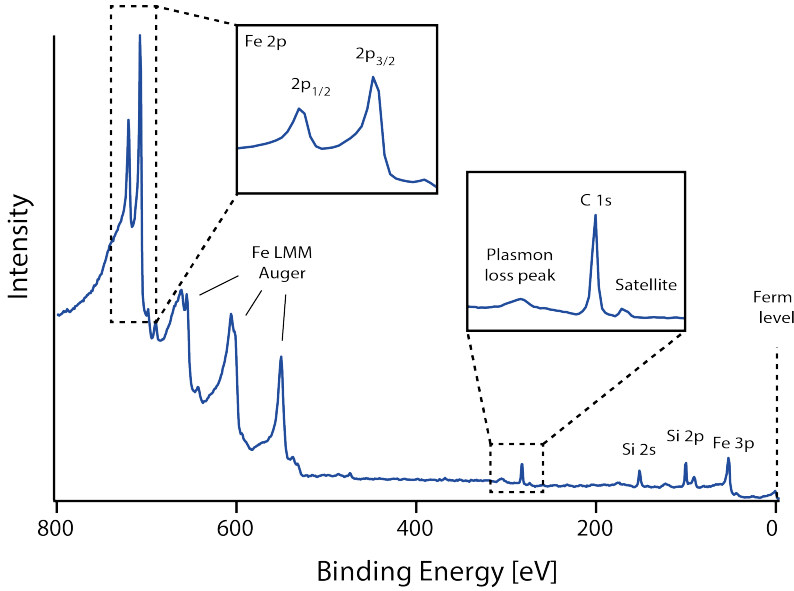

FIGURE 2.2: Mg Kα survey spectrum (widescan) of a SiC sample, with a Fe overlayer. Carbon and silicon core levels are clearly visible along with the plasmon loss peaks and satellites. In the Fe 2p core-level, a clear spin-orbit splitting is apparent. Fe LMM Auger peaks appear around 600 eV when using Mg Kα X-rays.

be used to confirm the presence of an element present in a sample in conjunction with the core-level peaks.

Spin-orbit splitting is a relativistic effect that is most prominent in heavier elements, and is caused by the interaction between the spin of an electron with its motion around the atomic nucleus. This effect splits the associated orbital energy in two, and produces two peaks in an XPS spectrum with an area ratio that depends on the number of electrons in each degenerate level [20].

2.1.2 Quantification and characterisation

There are several things that will broaden the peaks and limit the resolution of the technique. The X-ray source does not output a

perfectly monochromatic photon beam. Rather, it will have a Gaussian or Lorentzian distribution depending on the type of X-ray source [20]. Furthermore, photoelectrons will display an intrinsic Lorentzian line-shape which arises due to the core-hole lifetime, as well as thermal broadening due to atomic vibrations in the sample [26].

For a semiconductor a Voigt profile is commonly used to fit the core-level peaks. The Voigt line-shape is a convolution between the Gaussian and Lorentzian functions [20]. In a metal, the picture is a bit different. The photoelectron has to travel through a densely populated valence band, and can easily lose energy through Coulombic interaction with valence electrons in the metal, producing a strong asymmetry in the core-level peak. To fit this type of spectrum, a Doniach-Sunjic line shape is used, which takes the metallic nature of the sample into account in the model [27]. The degree of asymmetry gives information about the metallicity of the sample.

The intensity of the peaks depend on the photoionisation cross-section of the given orbital electron as well as the quantity of atoms present close to surface. The photons penetrate quite deep into the sample, however the photoelectrons has a very short attenuation length in comparison, so only the electrons closest to the surface will escape the sample. The intensity I of measured photoelectrons is attenuated according to

$$I = I_0 e^{-d/\lambda}, \tag{2.3}$$

where I_0 is the non-attenuated intensity, d is the depth at which the photoelectron originated in the solid and λ is the electron attenuation length. This can be used to determine the thickness of a grown overlayer by comparing the peak intensity before and after the depostion of a substance onto the surface. Usually λ is known and can be retrieved from tables [28].

When atoms form chemical bonds between one another, the change in the electronic structure will shift the binding energies of the core electrons by a certain amount. This shift is detectable in XPS, although some shifts are too small to be resolved by a common anode X-ray source. In these cases, synchrotrons are needed because of the highly monochromatic X-rays they generate. To analyse core-level peaks that display chemical shifts, multiple components in the fitting

function is often used. The number of components are not always apparent, since they may be close together. However, one may expect to see as many components as there are possible bonds. Often, a chi-square test is conducted to test the goodness of fit between the measured spectrum and the fitting function. If a good fit is achieved, one may infer the stoichiometry of molecules present in samples and track the formation of new species [29].

It is often necessary to remove the background signal generated by inelastically scattered photoelectrons when analysing core-level peaks. If a core-level peak is close to a neighbouring peak, their tails may overlap, complicating the peak fitting process. To subtract the background signal from the measured spectrum, a model of the physical processes that produce the background signal is used to estimate its shape. The background is subsequently subtracted from the spectrum. Common algorithms for background modelling are the Shirley background [30], and the Tougaard background [31]. However, there are several physical mechanisms contribute to the background signal, so there is a great deal of information about the system to be found in it.

2.2 Microscopy and diffraction

Spectroscopic analysis alone is not enough to fully characterise a surface. Often, XPS measurements are complemented by diffraction experiments and microscope imaging to gain information about the structure of the studied surface. LEEM can image surfaces with resolutions down to the nanometer scale. LEED gives detailed information about the crystallinity and long-range order of the surface structure, whilst PED images the diffraction patterns formed by photoelectrons. The SMART instrument used in this project (discussed in Chapter 3) has been shown to produce LEEM images with ~2.6 nm resolution [32].

2.2.1 Low-energy electron diffraction

LEED is based on the wave nature of electrons, and uses electrons to form a diffraction image of the sample surface. The de Broglie relationship relates the kinetic energy of an electron to its wavelength,

$$\lambda = \frac{h}{P}, \tag{2.4}$$

where h is Planck's constant and P is the momentum. Electrons with low energy have wavelengths that are similar to the typical interatomic distances in a solid, which is a condition for diffraction phenomena to occur. LEED is an extremely surface-sensitive technique due to the strong interaction of low-energy electrons with a crystal and the short attenuation length of electrons compared to that of X-rays. The technique gives direct information about the quality and order of the surface structure, as well as the types of symmetries and periodicities that are present.

In LEED, electrons with a certain kinetic energy (and therefore wavelength) are accelerated towards the sample, and the electrons scatter elastically off the surface atoms. Diffraction occurs because of constructive interference between the scattered electrons, and this happens when the Laue conditions are fulfilled [26]. The Laue conditions for the case of a two-dimensional lattice are

$$(\mathbf{k}_s^{\parallel} - \mathbf{k}_i^{\parallel}) = \Delta\mathbf{k}^{\parallel} = \mathbf{g} \tag{2.5}$$

where $\mathbf{k}_i^{\parallel}$ and $\mathbf{k}_s^{\parallel}$ are the components of the incident electron wave vector $\mathbf{k}_i$ and the scattered wave vector $\mathbf{k}_s$ that are parallel to the surface, and $\mathbf{g}$ is a reciprocal lattice vector.

The diffracted electrons form a diffraction pattern that maps out the reciprocal lattice structure of the surface. The diffraction pattern is imaged either by using a fluorescent screen and taking pictures of it with an ordinary camera, or by imaging the diffraction plane in an electron microscope. If the LEED apparatus is set up in such a way that the incident electron beam is normal to the sample surface ($\mathbf{k}_i^{\parallel} = 0$), then $\mathbf{k}_s^{\parallel} = \mathbf{g}$ and the diffraction maxima can be directly related to the reciprocal lattice vectors of the surface, which is often done to simplify the analysis.

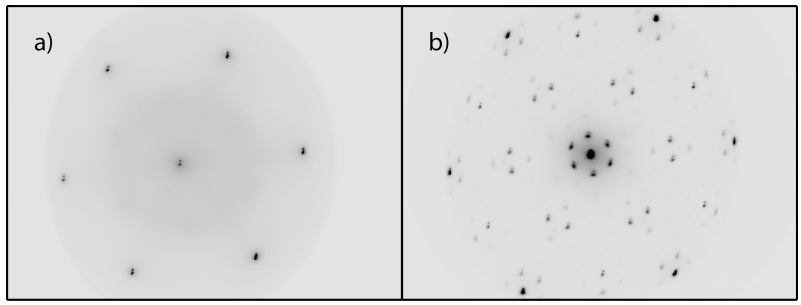

Figure 2.3: LEED patterns at 42 eV. **a)** Diffraction pattern taken for a clean SiC surface of high crystalline quality. The hexagonal surface structure is evident. **b)** A SiC surface with several surface structures of different orders and rotations relative to the substrate.

Figure 2.3a shows a LEED pattern taken from a clean SiC sample. The sharp diffraction spots indicate that the surface structure is of high crystalline quality, and the hexagonal structure of the reciprocal lattice is evident. In Figure 2.3b, several new spots have appeared, and are indicative of a surface with multiple domains. These domains may be rotated or stretched relative to the bulk structure.

The energy filtering capabilities of the SMART instrument enables imaging of diffraction patterns formed by photoelectrons emitted from the sample. This is photoelectron diffraction. By imaging the back focal plane which contains interference from all emission angles, the angular distribution of photoelectrons originating from the valence band of the sample can be imaged, if an appropriate photon energy is used. This gives information about the electronic structure of the sample near the surface, and can be used to "map" the valence band structure.

2.2.2 Low-energy electron microscopy

In LEEM, the diffracted electrons are used to form a high-resolution image of the sample surface. One diffraction spot is chosen for imaging, and all the electrons contributing to the intensity of the spot give rise to the contrast in the image [20]. Typically, the specularly

reflected beam (centre spot in LEED, see Figure 2.3) is used to form the image. This mode is called bright-field (BF) imaging. The contrast in BF mode is due to topographic features of the surface. If any of the other LEED spots are chosen for imaging, it is called dark field (DF) imaging. If a LEED pattern exhibits multiple crystal structures, one may choose one of the diffraction spots to see where the atoms with the corresponding structure are located on the surface.

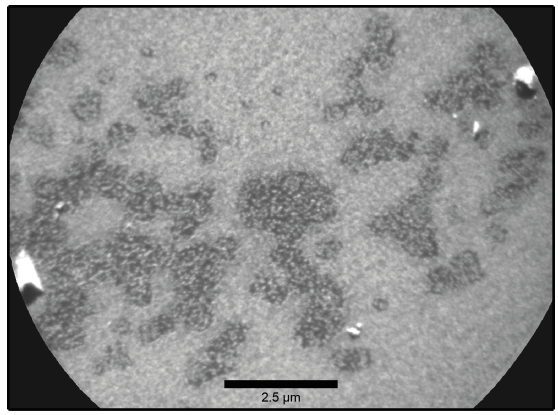

Figure 2.4: LEEM image taken with 50 eV electron energy in bright field mode. This sample has a non-uniform surface: multiple domains with differing crystal structures are visible, where the bright areas have the most well-ordered structures.

A LEEM image is shown of a surface in Figure 2.4. The contrast differences in the islands is due to the different diffraction intensities each island produces for the given electron energy. If the sample is kept at a slightly higher voltage than the electron source such that the electrons are reflected back without interfering with the sample surface, then the microscope is said to work in mirror electron microscopy (MEM) mode. MEM provides images for which the contrast is generated by topography and the work function. The reflected electrons are very sensitive to the topography and local electric fields because their low velocity close to the surface [33].

By varying the voltage at which the sample surface is held, it is possible to measure how the reflectivity of low-energy electrons

depend on the energy with which they interact with the sample. When the kinetic energy of the electrons exceed the work function of the sample, they will begin to interact with the surface, lowering the reflectivity. The reflectivity depends on the electronic structure of the surface and any grown materials, and will exhibit resonance at specific energies. Such resonances give information about the surface such as the number of grown graphene layers, for instance [34].

3 Instrumentation

In the last chapter, the principles behind the techniques used in this project were discussed. In this chapter the instrumentation required to perform the experiments are briefly discussed: the vacuum chamber, electron analysers, photon sources and means for growing FeSi and graphene. Experiments were performed at the BESSY II synchrotron in Berlin, Germany, and at the home lab in Trondheim.

3.1 Ultra-high vacuum

In experiments where the cleanliness of samples is important, the environment in which the experiments are performed also has to be clean. To prevent dust particles and smaller particles like stray molecules or atoms to accumulate on the sample surface, the sample can be placed in a vacuum chamber. The pressures required depend on the type of experiment: in XPS and LEEM/LEED experiments the pressure needs to be in the ultra-high vacuum (UHV) region which is at a pressure below $\sim 10^{-9}$ mbar. There are several reasons for this. Firstly, spectroscopic experiments are very sensitive, and any impurities that are present on a sample surface can clutter the measured spectra, or even attenuate signals that are important for the experiment. LEEM is even more sensitive. With the ability to resolve images at the nanometer scale, any dust or other impurity is likely to overshadow the surface under study. More importantly, the mean free path of photoelectrons and diffraction electrons must be long enough to travel between the sample and the detector without any significant loss of intensity. Secondly, the instrumentation of the XPS and LEEM/LEED techniques require very high electrical voltages, which can cause damaging sparks if the pressure in the vacuum chamber is too high.

The vacuum system has a series of pumps that are continuously running in order to maintain the low pressures. A roughing pump is used to initially pump the system down to a pressure of about 10^{-3}

mbar, where the air molecules no longer flow viscously [26]. At this point, a turbomolecular pump takes over, which has the capacity to reach the 10^{-11} mbar levels. The turbomolecular pump is used in conjunction with an ion pump in which the gas is being ionised by a high electric voltage. The ions are subsequently embedded in reactive targets in order to stop them from re-entering the vacuum chamber.

3.2 Photon sources

As mentioned above, the experiments were performed in two different facilities, one being the BESSY II synchrotron and the other the XPS lab at NTNU. There is a big difference in the quality and intensities of the photon beams generated in the two sources, and the operating principles are radically different.

The X-ray source at the NTNU lab is a twin anode X-ray gun. To generate the X-rays, a tungsten filament is heated such that thermionic electrons are emitted. The filament acts as a cathode, and the emitted electrons are accelerated using a high voltage towards a water-cooled metal anode [20]. The X-rays are generated when the thermionic electrons emitted from the filament excite electrons in the metal anode, which subsequently relax back to the ground state by releasing energy in the form of photons. Aluminium or magnesium anodes are commonly used, and it is possible to have multiple anodes installed in an X-ray lamp to allow the experimenter to switch between X-ray energies for convenience. Mg and Al anodes (used on our lab) have characteristic Kα emission at 1253.6 eV and 1486.6 eV, respectively [35].

The BESSY II synchrotron is an electron storage ring which produce X-rays of high brilliance. Electrons are accelerated from an electron gun by a linear accelerator into a dipole magnet synchrotron which ramps up the energy of the electron packets. When the electrons reach a certain energy, they are injected into the large storage ring which is equipped with undulators. The undulators are made up of a series of dipole magnets with alternating magnetic fields, which cause the electron packets to oscillate. Any charged particle that undergoes an acceleration at relativistic velocities will radiate

energy tangentially. In the undulator, the electron deflection paths are lined up such that the resulting radiation constructively interfere, producing an intense photon beam of high brilliance [36]. The UE49 undulator used in this project supplies photons in the energy range of 20 to 2000 eV (soft X-rays) [33]. The photon beam is sent through beamline optics towards the endstation. The beamline is equipped with a movable monochromator which allows the experimenter to tune the photon beam to the desired energies, unlike the anode X-ray gun in which the photon energy is fixed.

3.3 Electron analysers

To analyse the energies of photoelectrons that are emitted from samples, the electrons are collected by focusing lenses and sent through what is simply called an analyser. Two different types of analysers are used in this project: in the home lab at NTNU a "traditional" hemispherical electron analyser is employed; and at BESSY an integrated electron microscope with a so-called omega filter is used.

3.3.1 Hemispherical electron analyser

The hemispherical analyser consists of two concentric hemispheres that are set at a voltage difference, see Figure 3.1. When photoelectrons are ejected from the studied sample surface, they are collected and focused into the analyser by electrostatic lenses. When the electrons enter the analyser, the electric field in the hemisphere due to the voltage difference cause the electrons to disperse according to their kinetic energy distribution. The electrons that exactly follow a circular trajectory through the analyser have a kinetic energy that is determined by the pass energy of the system. The electrostatic lens system decelerate the electrons to the chosen pass energy, which is determined by the potential difference of the hemispheres. When acquiring a spectrum, the potential applied to the electrostatic lenses are scanned, which effectively scans the energy range of the emitted photoelectrons. After passing through the analyser, the electrons are detected by a CCD detector.

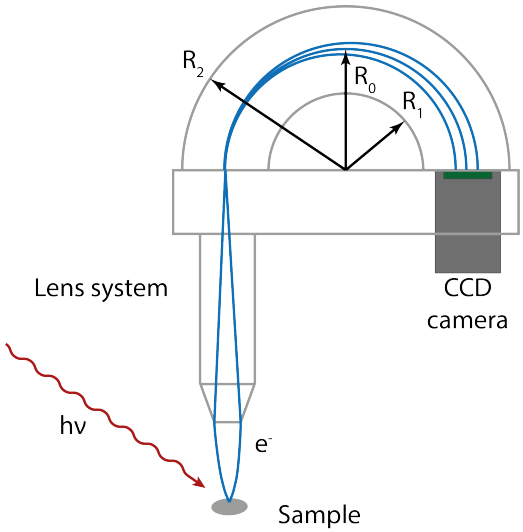

FIGURE 3.1: Hemispherical analyser. The sample is irradiated by X-rays, causing electrons to be emitted from the sample. The photoelectrons are focused into the hemisphere by an electrostatic lens system. A set voltage difference between the two hemispheres with radii R_1 and R_2 energy-filters the photoelectrons which are subsequently measured by the detector.

The resolution of the analyser is determined by the pass energy and the angular half aperture α of the electron beam which is determined by the lens system. The energy resolution ΔE is given by [20]

$$\Delta E = E_p \left(\frac{R_1 R_2}{2R_0 + \alpha^2} \right) \tag{3.1}$$

where R_0 is the mean radii of the hemispheres. In general, smaller pass energies will result in a higher energy resolution as is evident in Equation 3.1, but will also result in a lower electron transmission and thus increase the time needed to acquire data with good statistics. Thus, there is a trade-off between resolution and transmission. Often widescans are acquired at higher pass energies to reduce acquisition time since high resolution is less important. However, when recording data from specific core-levels, higher resolution is needed and the pass

energy is lowered. One would often do several sweeps for core-level scans to improve the signal-to-noise ratio.

3.3.2 The SMART instrument

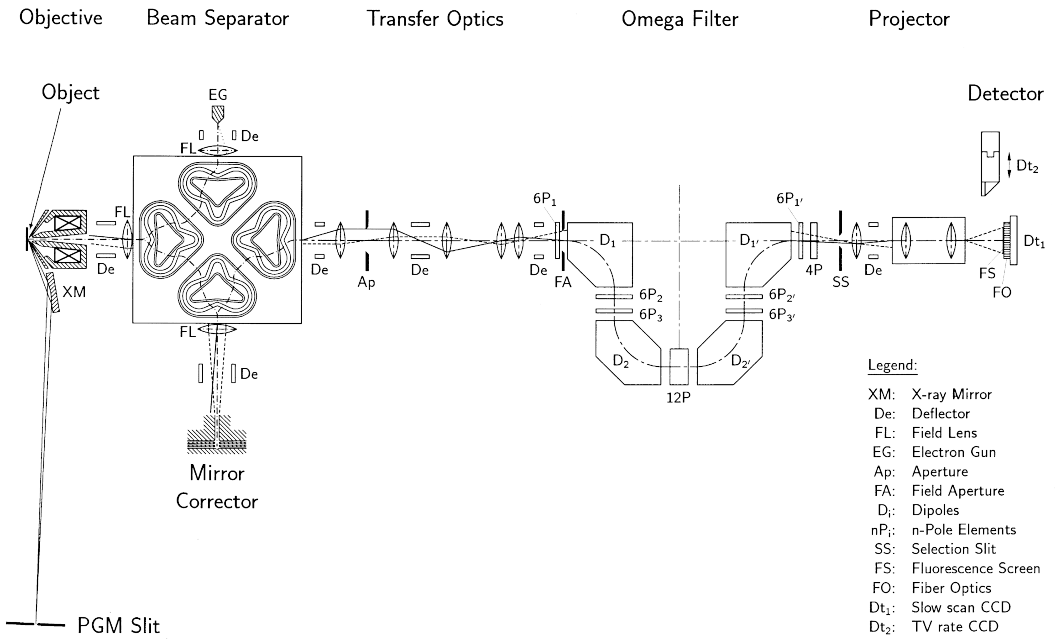

Figure 3.2: Schematic view of the SMART instrument [33].

The SMART instrument (SpectroMicroscope for All Relevant Techniques) is a spectromicroscope located at the UE49 soft X-ray beamline at the BESSY synchrotron. It has several operation modes, including XPS, LEEM, LEED and PED, discussed in Chapter 2.

A schematic overview of the SMART instrument can be seen in Figure 3.2. The sample is placed on the far left in the Figure. The monochromatic photon beam enters the instrument via an evacuated beamline (connecting the synchrotron to the endstation where the instrument is located) and is directed at the sample via a mirror. The electrons emitted from the sample due to the X-rays are collected by

the objective lens and enters the magnetic beam separator. The electrons are directed towards a tetrode mirror by the magnetic dipoles in the beam separator. The electrostatic mirror corrects for spherical and chromatic aberrations caused by the objective lens. After being reflected by the mirror, the electrons go through the beam separator and onwards through a series of electrostatic lenses (the transfer optics) where they arrive at the electron energy analyser. The analyser (called the "omega filter" due to its resemblance to the symbol Ω) filters the electrons by energy, much like the hemispherical electron analyser, and lets the energy-filtered electrons through to the CCD detector.

An electron gun is placed by the beam separator opposite the tetrode mirror, which allows the microscope to operate in LEEM and LEED modes as well as PEEM and XPS. Electrons emitted from the electron gun are directed towards the sample by the beam separator, which is made possible by the four-fold symmetry of the beam separator [33]. Subsequently, the electrons interact with the sample according to their energy.

3.4 E-beam evaporator

To coat samples with nanometer-thick films of metals, one needs to evaporate the metal source and closely control the growth rate on the sample. A common way of evaporating the metal sources is to use an electron beam (e-beam) evaporator, which works by bombarding a pure metal rod with energetic electrons. Electrons are emitted from a hot filament and are accelerated towards the tip of the metal rod by applying a high positive voltage on the rod. Metal is evaporated when the electrons hit the rod. The evaporator chamber is water-cooled to prevent outgassing and keep a very low working pressure.

The emission is controlled by adjusting the filament current (i.e. the temperature of the filament). When precise control over the deposited layer thickness is needed, metal is deposited at a low flux (often on a different sample) to calibrate the growth rate. A metal layer of a predetermined thickness can subsequently be deposited by carefully choosing the duration of the deposition process.

3.5 Sample cleaning

When growing thin films of any kind on a substrate, the sample cleanliness is vital for the quality of the grown film. Moreover, if graphene sheets of an appreciable size are to be produced, the substrate structure needs to be of high crystalline quality. This section outlines the main methods for cleaning the sample surfaces and ensuring good quality substrate structures.

Cleaning the surfaces by using chemicals and scrubbing them with cloths only removes dirt and impurities visible to the naked eye. A common method for minimising the amount of impurity adatoms present on the sample surface is ion sputtering. Typically, argon ions are accelerated towards the sample surface, which leaves the surface in a damaged, but cleaner state. The damaged state of the surface has to be repaired by heating, or annealing, the sample. By heating the sample to a high temperature, atoms in the crystal will be able to move around and cause the surface to reconstruct, leaving it in a ordered state. However, the annealing process may also cause impurity atoms within the bulk to migrate to the surface. Thus, it is often required to do several cycles of ion sputtering and annealing to obtain a clean and well-ordered surface suitable for thin-film growth.

4 Results and Discussion

Results from the experiments are presented in this chapter and are discussed consecutively. XPS experiments have been carried out in the home XPS lab at NTNU and LEED, LEEM and PED experiments were carried out at BESSY.

4.1 The clean SiC sample

To grow high quality graphene, a clean substrate of high crystalline quality is required. Thorough preparations and investigations were conducted on the bare 6H-SiC(0001) sample in order to ensure a good template for the Fe growth and subsequent graphene formation. The samples were subjected to ultrasonic washing for 10 minutes in ethanol in all experimental cases, then quickly blow-dried with dry nitrogen gas. The samples were subsequently put in the vacuum chamber and degassed at ~325° C until the pressure in the vacuum chamber recovered to ~1x10^{-9} mbar. The samples were then heated to ~800° C to reconstruct the surface before performing any analysis.

The results from the initial bare-surface SiC measurements are shown in Figure 4.1. The widescan in 4.1a) shows the sharp C 1s and Si 2s/2p core-level peaks in addition to a small amount of oxygen as seen from the O 1s and O KLL Auger peaks. Figure 4.1b) shows a high-resolution Si 2p spectrum taken at E_p = 20 eV. The Si 2p peak has been curve-fitted using two Voigt line-shapes to achieve a good fit, where **I** is located at 102.8 eV and **II** lies at a higher binding energy of 104.6 eV.

A LEED image of the sample surface taken at an electron energy of 45 eV is seen in Figure 4.2. The LEED image displays a sharp (1x1) hexagon pattern, indicating a highly crystalline surface.

Discussion of the clean surface results

The data in Figures 4.1 and 4.2 give clear indications of the cleanliness and structure of the surface. The diffraction pattern in Figure 4.2 is

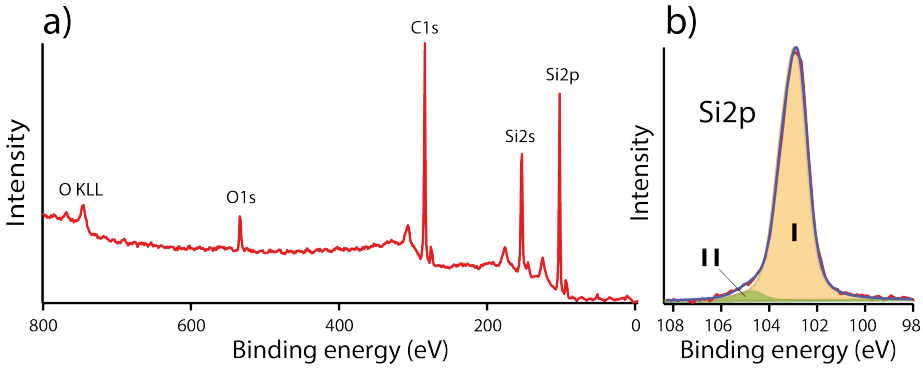

FIGURE 4.1: XPS spectra taken from a clean SiC surface using a Mg anode following preparatory annealing. **a)** Widescan. **b)** High-resolution spectrum from the Si 2p core-level, fitted with Voigt components for bulk SiC (**I**) and silicon oxide (**II**).

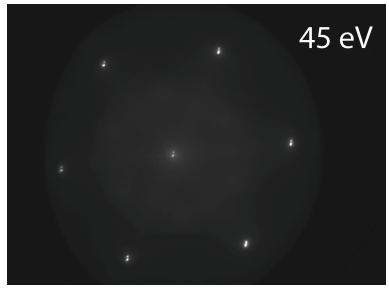

FIGURE 4.2: LEED image taken at a kinetic energy of 45 eV from the clean SiC surface following annealing.

consistent with the 6H-SiC(0001) structure seen in other studies [37]. The thorough degassing and subsequent high-temperature flashing seems to have cleared the sample of any atmospheric contaminants except for a small amount of oxygen. Component **I** in Figure 4.1b) is attributed to the SiC bulk [38], although a shift of ~1.2 eV towards higher binding energy can be seen. The second component located at a binding energy of 104.6 eV (component **II**) is due to an oxide film which has formed on the surface due to oxygen atoms bonding with

the silicon [39]. This component is also shifted by the same amount as **I**. Similar shifts were observed in C 1s core-level spectra (not shown), and are therefore assumed to be due to the sample charging as the photoelectrons leave the sample, as the charge neutralisation of the SiC bulk is limited [40]. The e-beam evaporator filament was turned on to flood the chamber with electrons in an attempt to replenish the sample, however with limited effect.

4.2 Deposition of iron

After the cleanliness and crystallinity of the SiC was verified, a thin Fe layer was deposited on the surface. Fe was deposited at 10 nA emission for a total of 50 min in room temperature. XPS, LEED and LEEM measurements were done to characterise the grown layer.

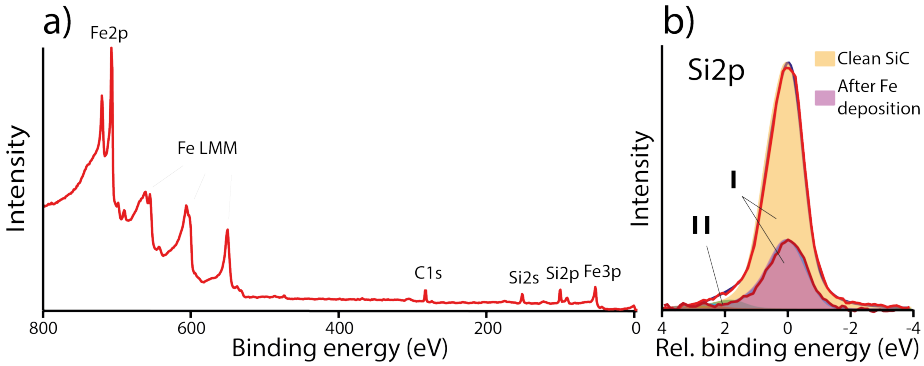

Figure 4.3: XPS measurements following Fe deposition. **a)** Widescan. **b)** High-resolution scan of the Si 2p core-level. The intensity of the Si 2p peak after Fe deposition (red) is compared with the intensity from a clean SiC sample (yellow). Voigt components from SiC (**I**) and SiO_2 (**II**) are included. The energy axis has been normalised to compensate for charging effects.

A widescan following the deposition of the Fe layer can be seen in Figure 4.3a). The spectrum is dominated by the Fe 2p and Fe LMM whilst the C and Si signals are attenuated by the Fe overlayer. The oxygen that was present before the Fe deposition is camouflaged by the Fe signal. A comparison between the Si 2p core-level before

(yellow peak) and after (purple peak) Fe deposition is shown in Figure 4.3b). The same components are used in the curve fitting. With the areas of the Si 2p peaks known, the thickness of the deposited Fe layer was determined to be ~1.5 nm using equation 2.3. A value for the electron attenuation length (EAL) λ was extracted from the NIST EAL database [41].

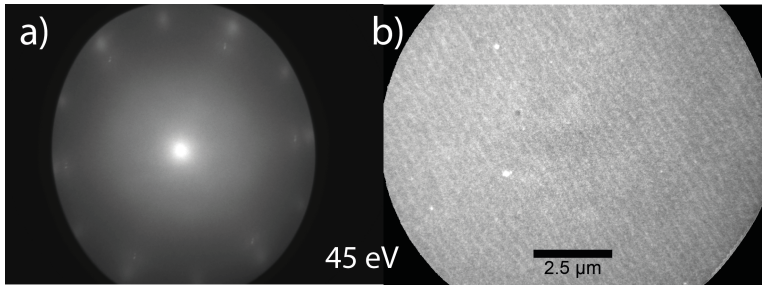

FIGURE 4.4: **a)** LEED image (45 eV) taken after Fe deposition. **b)** LEEM image with same electron energy taken of the surface following Fe deposition.

Figure 4.4 shows LEED and LEEM images (both 45 eV) of the surface following Fe deposition. The diffraction pattern produced by the surface is now more diffuse, indicating that the Fe layer is less ordered than the clean surface, although clear periodicities in the crystal structure must be present for diffraction to occur. The (1x1) hexagonal structure is still visible, but with additional spots further away from the centre spot. An extra 30° rotation can also be seen. The LEEM image in Figure 4.4b) indicates that the Fe layer is quite uniform, although straight lines are visible across the surface.

Discussion of iron deposition results

The growth of iron on the 6H-SiC(0001) surface has been investigated. The results from Figure 4.3 have shown that the thickness of the grown iron layer is ~1.5 nm, and the LEEM image shown in Figure 4.4b) show that the iron is uniformly distributed on the surface. Iron has been shown to grow layer by layer in similar conditions [20]. The lines that are visible in the LEEM could be arising due to terraces formed on the surface. The LEED pattern has some rotational domain

variations, although the overall structure of the iron surface is similar to that of 6H-SiC(0001). We therefore conclude that the iron layer is moderately well-ordered because good structural quality of the underlying SiC substrate.

4.3 FeSi formation

The iron layer lowers the activation energy for graphene formation on SiC. Carbon atoms travel through the iron layer to the surface to form graphene during annealing, whilst the remaining silicon atoms bond with the iron to form FeSi of different phases. To initiate the graphitisation process (and thus the FeSi formation), the samples with the grown iron layers were annealed at regular temperature intervals. The samples were cooled down between each annealing step for XPS measurements, and the results are presented below.

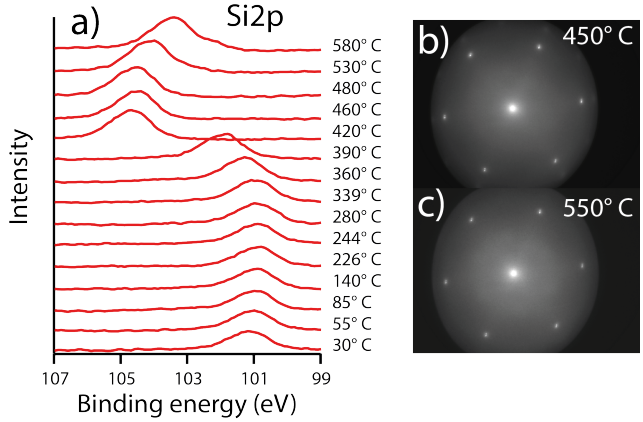

Figure 4.5: XPS and LEED data taken during the annealing process. **a)** The evolution of the Si 2p core-level with annealing. The shifts in binding energy occur when the sample becomes positively charged with the loss of photoelectrons. **b)** and **c)** LEED patterns (45 eV) after reaching 450° and 550° C, respectively.

Figure 4.5 shows the results from the annealing process. In a), the evolution of the Si 2p core-levels are shown, displaying shifts towards

higher binding energies as the sample heats up. At 30° C the peak centre is located at 101.2 eV. It shifts to 100.9 eV at around 225° C, 104.7 eV at 420° C and finally 103.4 eV when reaching 580° C. In Figure 4.5b) and c), the LEED pattern is shown for temperatures of 450° and 550° C, respectively. The diffraction patterns indicate that the iron surface has reconstructed to match the structure of SiC. Since the structural quality of the grown graphene layer strongly depends on the crystallinity of the substrate, the good structural quality of the iron layer should provide excellent conditions for the formation of high quality graphene.

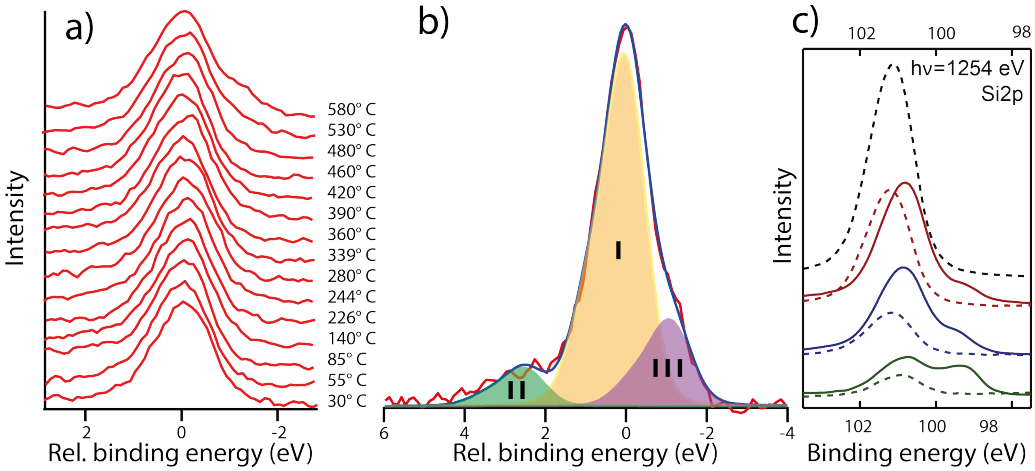

Figure 4.6: Results from annealing steps done on SiC with a Fe overlayer. **a)** Evolution of Si 2p core-levels with temperature, revealing a new peak shoulder after 480° C. **b)** High-resolution scan of the Si 2p core-level, showing a new component (**III**) formed after annealing. **I** and **II** are Si 2p components from SiC and SiO_2 environments, respectively. The energy scaling has been normalised to compensate for charging. **c)** Si 2p core-level spectra taken for a clean SiC surface (black dashed line), SiC + Fe (coloured dashed lines) and annealed SiC + Fe (coloured solid lines) for Fe thicknesses of 0.4 nm (red), 1 nm (blue) and 3 nm (green). Lower binding energies correspond to silicide formation. Adapted from [15], for reference.

In Figure 4.6a), the Si 2p core-level peaks are aligned to highlight a shoulder emerging after the sample was annealed to ~480° C. A

high-resolution spectrum of the Si 2p peak at 580° C is shown in Figure 4.6b), where the peak has been fitted with three Voigt components. Component **I** and **II** are the same as before (SiC and SiO_2, respectively), and **III** is the shoulder emerging in a) and is attributed to FeSi formation. Component **III** has 1.2 eV lower binding energy than **I**, and accounts for about 25% of the total peak intensity. A reference figure showing the Si 2p peak in SiC during annealing with and without an iron layer is shown in Figure 4.6c), included for comparison [15]. Solid lines are annealed SiC + Fe, and display the same general shapes as the data presented in a) and b).

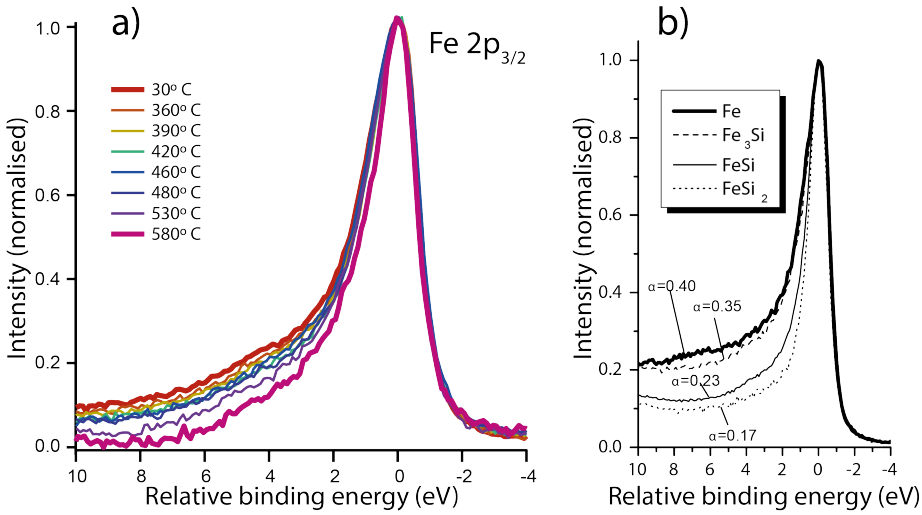

FIGURE 4.7: Fe $2p_{3/2}$ spectra, normalised to the peak heights. The energy scales are also normalised with respect to the Fe $2p_{3/2}$ centre. **a)** Evolution of the asymmetry factor in Fe $2p_{3/2}$ spectra with annealing. **b)** Asymmetry of the Fe $2p_{3/2}$ peak for Fe and different FeSi phases. Adapted from [42] for reference.

A normalised high-resolution scan of the Fe $2p_{3/2}$ core-level is shown in Figure 4.7a), showing how the shape changes with increasing temperature. The peak is seen to become narrower and more symmetric as the sample is annealed. A reference figure is included in Figure 4.7b) where the asymmetry of the Fe $2p_{3/2}$ core-level peak

is shown for pure Fe and different phases of FeSi [42]. This is a good indicator that the iron layer becomes less metallic when it starts to bond with silicon from the substrate.

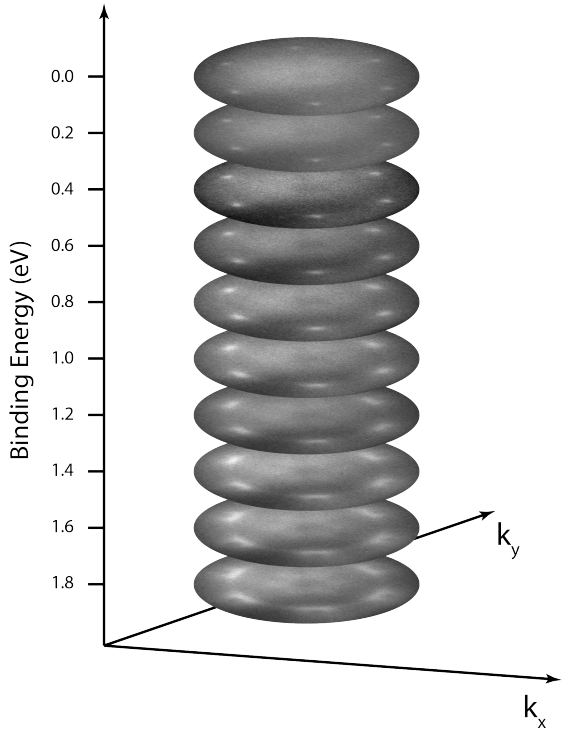

FIGURE 4.8: Constant energy slices showing the conical π bands of graphene, starting from the top of the valence band (top, 0 eV) going down to 1.8 eV binding energy (bottom).

In Figure 4.8, stacked constant energy slices of the valence band is shown, revealing formation of graphene on the surface. The conical bands of graphene's π states are visible at increasing binding energy (see also Figure 1.1). Thus, graphene has already formed on the surface before reaching the previous reported temperature of 600° C [15].

Discussion of FeSi formation results

The annealing process of SiC + Fe has been monitored using XPS, LEED and LEEM, and has allowed us to track the formation of a FeSi interlayer during graphene growth.

As seen in Figure 4.6a), the annealing produces a distinct shoulder in the Si 2p core-level spectra, which signifies the onset of graphitisation and hence FeSi formation. The binding energy of photoelectrons from Fe-bonded silicon are known from other experiments [15, 43], and match the binding energy of component **III** in Figure 4.6b). A very weak signal from component **III** first becomes visible after annealing the sample to 390° C, suggesting that the FeSi starts forming around these temperatures. However, the asymmetry factor of the Fe $2p_{3/2}$ core-level spectra in Figure 4.7 seems to become smaller already at 360° C. This suggests that the iron atoms gradually starts breaking up Si-C bonds in the substrate to form Fe-Si bonds before a quantifiable XPS signal from the Si 2p core-level can be seen in the spectrum.

Figure 4.7 shows that the asymmetry factor in the Fe $2p_{3/2}$ decreases as the annealing temperature increases. The asymmetry factor of the Fe $2p_{3/2}$ spectra depends on the FeSi phase, as can be seen in Figure 4.7b) [42]. Previous studies performed on Fe-mediated graphene growth on SiC in similar conditions have found that the dominant phase is in fact FeSi, although with the possibility of small amounts of $FeSi_2$ occurring [15]. Therefore, the Fe $2p_{3/2}$ core-level is approaching that of the FeSi spectrum in Figure 4.7b). The peak tails in the two Fe $2p_{3/2}$ spectra are slightly different, because different anodes were used in the respective X-ray sources.

The LEED pattern in Figure 4.5b) was taken after the sample had annealed to 450° C. The iron surface has reconstructed to match the hexagonal structure of the 6H-SiC(0001) surface, although weak diffraction spots can still be seen near the outer edges of the diffraction pattern. Thus, the crystal structure is of good quality before graphitisation occurs, with a few 30° rotations. After annealing the sample to 550° (Figure 4.5b)), all other diffraction spots have disappeared, leaving only the (1x1) structure of SiC. When the SiC + Fe system is annealed, carbon atoms migrate through the iron layer as

the Fe atoms bond with Si, forming graphene on the resulting FeSi surface. Since the iron layer is seen here to reconstruct into epitaxial Fe before graphitisation occurs, it means that the formed FeSi interlayer is structured in register with the substrate, which greatly improves the quality of the grown graphene film.

The asymmetry factor arising in XPS core-level spectra taken from metallic samples is due to the high DOS at the valence band, as discussed in Chapter 2. As seen in Figure 4.7a), the asymmetry in the Fe $2p_{3/2}$ becomes smaller with increasing temperature, thus reducing the DOS at the Fermi level in the iron layer, which in turn affect the conductivity of the material. In Figure 4.5a), the charging effect in the sample becomes more pronounced after reaching 420° C. Moreover, the asymmetry in the measured Fe $2p_{3/2}$ spectra has already started to become smaller at this temperature. This means that there is an insulating layer forming in the sample before the main FeSi phase becomes visible in the Si 2p spectra. One can already see that the binding energy begin to shift towards higher energies at 390° C, although the addition of a FeSi component did not improve the curve fit at this temperature. Thus, the insulating layer is forming at the SiC-Fe interface, whence the photoelectrons from the FeSi component would be attenuated by the iron overlayer and otherwise dominated by the bulk SiC component. Since the FeSi interlayer is seen to be electrically insulating, it would simplify the fabrication of the proposed radiation sensor by providing the required insulating layer "for free" when growing the graphene film.

When the sample is annealed to ~530° C, the Si 2p core-level seems to shift back towards lower binding energy, indicating that the sample again becomes more conductive. The constant energy slices in Figure 4.8 display a graphene-like band structure, which is a clear sign that few-layer graphene sheets has formed on the surface. The graphene conducts electrons back into the sample, thereby neutralising the charging. The low graphitisation temperature observed here is rather surprising, as previous studies have seen that the graphitisation process begins closer to 600° C using this method, and untreated SiC surfaces will only start to decompose into graphene at around 1300° C. Since controlled graphene formation at such high temperatures

is not viable for commercial fabrication, the reduction in activation temperature due to the iron layer could enable large-scale production of graphene-based devices in the industry.

5 Conclusion

In this project, the FeSi interlayer formed when growing graphene by annealing Fe-treated 6H-SiC(0001) substrates has been studied. The purpose of this work was to characterise the SiC-FeSi-$C_{graphene}$ system in order to determine its feasibility as a device for radiation detection. The main goal was to determine the annealing temperature at which the FeSi interlayer formation begins, and whether it provides good enough electrical insulation between the SiC substrate (the radiation absorber) and the graphene (the sensor). Experiments were carried out using X-ray photoelectron spectroscopy, low-energy electron diffraction and microscopy as well as photoemission diffraction.

The onset of graphitisation and FeSi formation was found to occur at a temperature of ~390° C, although a clear XPS signal from FeSi components appeared only after the sample was annealed to 420° C. This is a rather large reduction of the graphitisation temperature compared to the bare SiC surface. Furthermore, the iron layer displayed a high crystalline quality after the sample was annealed to 450° C, such that the resulting graphene formed on top of the FeSi also was of pristine quality. This could make production of high quality graphene more accessible to commercial fabrication. Moreover, the sample became positively charged with the loss of photoelectrons after the FeSi formation had begun, and the asymmetry factor (characteristic of a metallic material) became smaller as iron atoms bonded with silicon to form FeSi, indicating that the FeSi interlayer is indeed insulating. This result means that the radiation sensor grows itself: by simply heating up the SiC + Fe system, a high quality graphene film is formed on top of a well-ordered insulating interlayer, as described in Chapter 1.

Future studies may further characterise the SiC-FeSi-$C_{graphene}$ system by studying the dependence on the annealing speed and duration, in addition to accurately quantifying the asymmetry factor of Fe $2p_{3/2}$ core-level in order to determine the quantity of other FeSi phases produced. The difference between the graphitisation temperatures for

Fe-treated and untreated SiC surfaces enables grown graphene films to be patterned by masking or lithography. This could open up the possibility for making pixelated graphene sensors which adds spatial resolution to the detector system.

Bibliography

[1] K. S. Novoselov, A. K. Geim, S. V. Morozov, D. Jiang, Y. Zhang, S. V. Dubonos, I. V. Grigorieva, and A. A. Firsov. «Electric field effect in atomically thin carbon films.» en. In: *Science (New York, N.Y.)* 306.5696 (Oct. 2004), pp. 666–669. ISSN: 1095-9203. DOI: 10.1126/science.1102896 (cit. on p. 1).

[2] A. K. Geim and K. S. Novoselov. «The rise of graphene.» In: *Nature materials* 6.3 (Mar. 2007), pp. 183–91. ISSN: 1476-1122. DOI: 10.1038/nmat1849 (cit. on p. 1).

[3] I. Ovid'ko. «Mechanical Properties of Graphene». In: *Reviews on Advanced Materials Science* 34 (2013), pp. 1–11 (cit. on p. 1).

[4] A. A. Balandin. «Thermal properties of graphene and nanostructured carbon materials.» In: *Nat. Mater.* 10.8 (2011), p. 569. ISSN: 1476-1122. DOI: 10.1038/nmat3064. arXiv: 1106.3789 (cit. on p. 1).

[5] A. H. Castro Neto, F. Guinea, N. M. R. Peres, K. S. Novoselov, and A. K. Geim. «The electronic properties of graphene». In: *Reviews of Modern Physics* 81.1 (2009), pp. 109–162. ISSN: 00346861. DOI: 10.1103/RevModPhys.81.109. arXiv: 0709.1163 (cit. on p. 1).

[6] P. Wallace. «The Band Theory of Graphite». In: *Physical Review* 71.9 (May 1947), pp. 622–634. ISSN: 0031-899X. DOI: 10.1103/PhysRev.71.622 (cit. on p. 1).

[7] K. S. Novoselov, A. K. Geim, S. V. Morozov, D. Jiang, M. I. Katsnelson, I. V. Grigorieva, S. V. Dubonos, and A. A. Firsov. «Two-dimensional gas of massless Dirac fermions in graphene». In: *Nature* 438.7065 (2005), pp. 197–200. ISSN: 0028-0836. DOI: 10.1038/nature04233. arXiv: 0509330 [cond-mat] (cit. on p. 1).

[8] S. Y. Zhou, G.-H. Gweon, J. Graf, A. V. Fedorov, C. D. Spataru, R. D. Diehl, Y. Kopelevich, D.-H. Lee, S. G. Louie, and A. Lanzara. «First direct observation of Dirac fermions in graphite». In: *Nature Physics* 2.September (2006), pp. 595–599. issn: 1745-2473. doi: 10.1038/nphys393. arXiv: 0608069 [cond-mat] (cit. on p. 1).

[9] M. Foxe, S. Member, G. Lopez, I. Childres, R. Jalilian, C. Roecker, J. Boguski, I. Jovanovic, and Y. P. Chen. «Detection of Ionizing Radiation Using Graphene Field Effect Transistors». In: *IEEE Transactions on Nanotechnology* 11 (2012) (cit. on pp. 1, 3).

[10] A. Patil, O. Koybasi, G. Lopez, M. Foxe, I. Childres, C. Roecker, J. Boguski, J. Gu, M. L. Bolen, M. A. Capano, I. Jovanovic, P. Ye, Y. P. Chen, and M. A. Bolen. «Graphene field effect transistor as radiation sensor». In: *IEEE Nuclear Science Symposium Conference Record* (2012), pp. 455–459. issn: 10957863. doi: 10.1109/NSSMIC.2011.6154538 (cit. on p. 3).

[11] O. Koybasi, I. Childres, I. Jovanovic, and Y. Chen. «Design and Simulation of a Graphene DEPFET Detector». In: *IEEE Nuclear Science Symposiwn and Medical Imaging Conference Record* (2012), pp. 4249–4254 (cit. on p. 3).

[12] W. A. de Heer, C. Berger, X. Wu, P. N. First, E. H. Conrad, X. Li, T. Li, M. Sprinkle, J. Hass, M. L. Sadowski, M. Potemski, and G. Martinez. «Epitaxial graphene». In: *Solid State Communications* 143.1-2 (2007), pp. 92–100. issn: 00381098. doi: 10.1016/j.ssc.2007.04.023. arXiv: 0704.0285 (cit. on p. 3).

[13] N. Tokuda, M. Fukui, T. Makino, D. Takeuchi, S. Yamsaki, and T. Inokuma. «Formation of graphene-on-diamond structure by graphitization of atomically flat diamond (111) surface». In: *Japanese Journal of Applied Physics* 52.11 PART 1 (2013). issn: 00214922. doi: 10.7567/JJAP.52.110121 (cit. on p. 3).

[14] S. B. Colbran. *Element Six CVD Diamond Handbook*. 2015 (cit. on p. 4).

[15] S. P. Cooil, F. Song, G. T. Williams, O. R. Roberts, D. P. Langstaff, B. Jørgensen, K. Høydalsvik, D. W. Breiby, E. Wahlström, D. A. Evans, and J. W. Wells. «Iron-mediated growth of epitaxial graphene on SiC and diamond». In: *Carbon* 50.14 (2012), pp. 5099–5105. issn: 00086223. doi: 10.1016/j.carbon.2012.06.050 (cit. on pp. 4, 28–31).

[16] S. P. Cooil, J. W. Wells, D. Hu, Y. R. Niu, A. A. Zakharov, M. Bianchi, and D. A. Evans. «Controlling the growth of epitaxial graphene on metalized diamond (111) surface». In: *Applied Physics Letters* 107.18 (2015). issn: 00036951. doi: 10.1063/1.4935073 (cit. on p. 4).

[17] J. B. Casady and R. W. Johnson. «Status of silicon carbide (SiC) as a wide-bandgap semiconductor for high-temperature applications: a review». In: *Solid State Electronics* 39.96 (1996), pp. 1409–1422 (cit. on p. 4).

[18] Y. Mizokawa, S. Nakanishi, and S. Miyase. «AES Study of the Reaction between a Thin Fe-Film and b-SiC (100) Surface». In: *Japanese Journal of Applied Physics* 28.12 (1989), pp. 2570–2575 (cit. on p. 4).

[19] C. N. Berglund and W. E. Spicer. «Photoemission studies of copper and silver: Theory». In: *Physical Review* 136.4A (1964). issn: 0031899X. doi: 10.1103/PhysRev.136.A1030 (cit. on p. 5).

[20] S. P. Cooil. «Controlling the Epitaxial Growth of Graphene On Diamond Surfaces». PhD thesis. Aberystwyth University, 2014. isbn: 9780708320051 (cit. on pp. 5–9, 13, 16, 18, 26).

[21] A. Einstein. «On a Heuristic Viewpoint Concerning the Production and Transformation of Light». In: *Annalen der Physik* 17.6 (1905), pp. 132–148. issn: 00033804. doi: 10.1002/andp.19053220607 (cit. on p. 6).

[22] F. Reinert and S. Hüfner. «Photoemission spectroscopy - From early days to recent applications».
In: *New Journal of Physics* 7 (2005). ISSN: 13672630.
DOI: 10.1088/1367-2630/7/1/097 (cit. on pp. 6, 7).

[23] P. A. M. Dirac. «The Quantum Theory of the Emission and Absorption of Radiation». In: *Proceedings of the Royal Society of London A* 114.767 (1927), pp. 243–265. ISSN: 1364-5021.
DOI: 10.1098/rspa.1983.0054 (cit. on p. 7).

[24] R. A. Pollak, L. Ley, F. R. McFeely, S. P. Kowalczyk, and D. A. Shirley. «Characteristic energy loss structure of solids from x-ray photoemission spectra».
In: *Journal of Electron Spectroscopy and Related Phenomena* 3.5 (Jan. 1974), pp. 381–398. ISSN: 03682048.
DOI: 10.1016/0368-2048(74)80022-8 (cit. on p. 7).

[25] L. Meitner. «Über die Entstehung der ß-Strahl-Spektren radioaktiver Substanzen».
In: *Zeitschrift für Physik* 9.1 (Dec. 1922), pp. 131–144.
ISSN: 14346001. DOI: 10.1007/BF01326962 (cit. on p. 7).

[26] P. Hofmann. *Surface Physics*. 2013 (cit. on pp. 9, 11, 16).

[27] S. Doniach and M. Sunjic. «Many-electron singularity in X-ray photoemission and X-ray line spectra from metals». In: *Journal of Physics C: Solid State Physics* 3.2 (1970), pp. 285–291.
ISSN: 0022-3719. DOI: 10.1088/0022-3719/3/2/010
(cit. on p. 9).

[28] M. P. Seah and W. A. Dench.
«Quantitative electron spectroscopy of surfaces: A standard data base for electron inelastic mean free paths in solids».
In: *Surface and Interface Analysis* 1.1 (1979), pp. 2–11
(cit. on p. 9).

[29] F. Mazzola. «Photoemission spectroscopies and their application in solid state and material physics». PhD thesis. Norwegian University of Science and Technology, 2016.
ISBN: 9788232615322 (cit. on p. 10).

[30] J. Végh. «The Shirley background revised». In: *Journal of Electron Spectroscopy and Related Phenomena* 151.3 (2006), pp. 159–164. ISSN: 03682048. DOI: 10.1016/j.elspec.2005.12.002 (cit. on p. 10).

[31] S. Tougaard. «Quantitative analysis of the inelastic background in surface electron spectroscopy». In: *Surface and Interface Analysis* 11.October 1987 (1988), pp. 453–472. ISSN: 0142-2421. DOI: 10.1002/sia.740110902 (cit. on p. 10).

[32] T. Schmidt, H. Marchetto, P. L. Lévesque, U. Groh, F. Maier, D. Preikszas, P. Hartel, R. Spehr, G. Lilienkamp, W. Engel, R. Fink, E. Bauer, H. Rose, E. Umbach, and H. J. Freund. «Double aberration correction in a low-energy electron microscope». In: *Ultramicroscopy* 110.11 (2010), pp. 1358–1361. ISSN: 03043991. DOI: 10.1016/j.ultramic.2010.07.007 (cit. on p. 10).

[33] R. Fink, M. Weiss, E. Umbach, D. Preikszas, H. Rose, R. Spehr, P. Hartel, W. Engel, R. Degenhardt, R. Wichtendahl, H. Kuhlenbeck, W. Erlebach, K. Ihmann, R. Schlögl, H.-J. Freund, a.M. Bradshaw, G. Lilienkamp, T. Schmidt, E. Bauer, and G. Benner. «SMART: a planned ultrahigh-resolution spectromicroscope for BESSY II». In: *Journal of Electron Spectroscopy and Related Phenomena* 84 (1997), pp. 231–250. ISSN: 03682048. DOI: 10.1016/S0368-2048(97)00016-9 (cit. on pp. 13, 17, 19, 20).

[34] H. Hibino, H. Kageshima, F. Maeda, M. Nagase, Y. Kobayashi, and H. Yamaguchi. «Microscopic thickness determination of thin graphite films formed on SiC from quantized oscillation in reflectivity of low-energy electrons». In: *Physical Review B - Condensed Matter and Materials Physics* 77.7 (2008), pp. 1–7. ISSN: 10980121. DOI: 10.1103/PhysRevB.77.075413. arXiv: 0710.0469 (cit. on p. 14).

[35] A. C. Thompson, D. T. Attwood, E. M. Gullikson, M. R. Howells, J. B. Kortright, A. L. Robinson, J. H. Underwood, K.-J. Kim, J. Kirz, I. Lindau, P. Pianetta,

H. Winick, G. P. Williams, and J. H. Scofield.
X-ray data booklet. Vol. 8. 4. 2001, p. 1125.
isbn: LBNL/PUB-490 Rev. 3.
doi: 10.1107/S090904950100807X (cit. on p. 16).

[36] J. Als-Nielsen and D. McMorrow.
Elements of Modern X-ray Physics: Second Edition. 2011.
isbn: 9780470973950. doi: 10.1002/9781119998365
(cit. on p. 17).

[37] C. Berger, Z. Song, T. Li, X. Li, A. Y. Ogbazghi, R. Feng, Z. Dai, N. Alexei, M. E. H. Conrad, P. N. First, and W. A. De Heer.
«Ultrathin epitaxial graphite: 2D electron gas properties and a route toward graphene-based nanoelectronics». In: *Journal of Physical Chemistry B* 108.52 (2004), pp. 19912–19916.
issn: 15206106. doi: 10.1021/jp040650f.
arXiv: 0410240 [cond-mat] (cit. on p. 24).

[38] E. Rollings, G. H. Gweon, S. Y. Zhou, B. S. Mun, J. L. McChesney, B. S. Hussain, A. V. Fedorov, P. N. First, W. A. de Heer, and A. Lanzara.
«Synthesis and characterization of atomically thin graphite films on a silicon carbide substrate». In: *Journal of Physics and Chemistry of Solids* 67.9-10 (2006), pp. 2172–2177.
issn: 00223697. doi: 10.1016/j.jpcs.2006.05.010.
arXiv: 0512226 [cond-mat] (cit. on p. 24).

[39] F. Esaka, H. Yamamoto, N. Matsubayashi, Y. Yamada, M. Sasase, K. Yamaguchi, S. Shamoto, M. Magara, and T. Kimura. «X-ray photoelectron and X-ray absorption spectroscopic study on ß-FeSi2 thin films fabricated by ion beam sputter deposition».
In: *Applied Surface Science* 256.10 (2010), pp. 3155–3159.
issn: 01694332. doi: 10.1016/j.apsusc.2009.11.090
(cit. on p. 25).

[40] W. M. Lau.
«Use of surface charging in x-ray photoelectron spectroscopic studies of ultrathin dielectric films on semiconductors».

In: *Applied Physics Letters* 54.4 (1989), pp. 338–340. ISSN: 00036951. DOI: 10.1063/1.101450 (cit. on p. 25).

[41] C. J. Powell and A. Jablonski. *NIST Electron Effective-Attenuation-Length Database*. 1.3. Gaithersburg, MD: National Institute of Standards and Technology, 2011 (cit. on p. 26).

[42] N. Ohtsu, M. Oku, K. Satoh, and K. Wagatsuma. «Dependence of core-level XPS spectra on iron silicide phase». In: *Applied Surface Science* 264 (2013), pp. 219–224. ISSN: 01694332. DOI: 10.1016/j.apsusc.2012.09.176 (cit. on pp. 29–31).

[43] M. Gomoyunova, D. Malygin, I. Pronin, a.S. Voronchikhin, D. Vyalikh, and S. Molodtsov. «Initial stages of iron silicide formation on the Si(100)2×1 surface». In: *Surface Science* 601.21 (2007), pp. 5069–5076. ISSN: 00396028. DOI: 10.1016/j.susc.2007.09.007 (cit. on p. 31).